mathematics

MDPI

Article

Low-Temperature Industrial Waste Heat (IWH) Recovery Using a New Design for Fast-Charging Thermal Energy Storage Units

Mehdi Ghalambaz [1,2,*], Hani Abulkhair [3,4], Obai Younis [5,6], Mehdi Fteiti [7], Ali J. Chamkha [8], Iqbal Ahmed Moujdin [3,4] and Abdulmohsen Omar Alsaiari [3,4]

1 Institute of Research and Development, Duy Tan University, Da Nang 550000, Vietnam
2 Faculty of Electrical—Electronic Engineering, Duy Tan University, Da Nang 550000, Vietnam
3 Center of Excellence in Desalination Technology, King Abdulaziz University, Jeddah 21589, Saudi Arabia
4 Mechanical Engineering Department, King Abdulaziz University, Jeddah 21589, Saudi Arabia
5 Department of Mechanical Engineering, College of Engineering in Wadi Addwasir, Prince Sattam Bin Abdulaziz University, Al-Kharj 11942, Saudi Arabia
6 Department of Mechanical Engineering, Faculty of Engineering, University of Khartoum, Khartoum 11111, Sudan
7 Physics Department, Faculty of Applied Science, Umm Al-Qura University, Makkah 24381, Saudi Arabia
8 Faculty of Engineering, Kuwait College of Science and Technology, Doha 35004, Kuwait
* Correspondence: mehdighalambaz@duytan.edu.vn

Abstract: The dynamic melting of CuO–coconut oil was addressed in a latent-heat thermal energy storage unit loaded with copper foam. In a new design, the thermal storage unit is made of a shell-tube-shaped chamber, in which a liquid flow of hot phase-change material (PCM) is allowed to enter the chamber from a port at the bottom and exit at the top. A fin is mounted in the chamber to forward the entrance PCM liquid toward the solid regions. The control equations were solved using the finite element method. The impact of foam porosity, inlet pressure, fin length, and the concentrations of CuO nanoparticles on the thermal charging time of the chamber was investigated. A fast-charging time of 15 min with a foam porosity of 0.95 was achieved. A porosity of 0.95 can provide a maximum thermal charging power of 15.1 kW/kg. The inlet pressure was a significant parameter, and increasing the inlet pressure from 0.5 kPa to 4 kPa reduced the melting time by 2.6 times. The presence of the fin is not advantageous, and even a long fin could extend the thermal charging time. Moreover, dispersed nanoparticles were not beneficial to dynamic melting and extended the thermal charging time.

Keywords: dynamic melting; open latent-heat thermal energy storage; CuO–coconut oil phase-change material

MSC: 76R10; 80A22

Citation: Ghalambaz, M.; Abulkhair, H.; Younis, O.; Fteiti, M.; Chamkha, A.J.; Moujdin, I.A.; Alsaiari, A.O. Low-Temperature Industrial Waste Heat (IWH) Recovery Using a New Design for Fast-Charging Thermal Energy Storage Units. *Mathematics* **2023**, *11*, 153. https://doi.org/10.3390/math11010153

Academic Editors: Siti Diana Nabilah Mohd Nasir, Eng Ofetotse and Bukunmi Ogunsanya

Received: 8 December 2022
Revised: 21 December 2022
Accepted: 23 December 2022
Published: 28 December 2022

1. Introduction

A significant factor in minimizing air pollution and global warming is substituting fossil fuels with renewable energies [1]. For these types of energy to overcome the drawbacks of inconsistent energy supply and demand, as well as space/time inconsistencies, thermal energy storage (TES) is of vital importance [2]. There are three types of TES: sensible, latent heat, and thermochemical [3]. Latent-heat TES (LHTES) shows high heat storage capacity per unit volume without significant temperature variations compared to the two others [4]. The most common application of LHTES is the combination of shell-tube heat exchangers and phase-change materials (PCMs) [5]. In this type of TES, the most critical disadvantage is the low thermal conductivity of the PCMs; it precludes the efficient storage and conversion of energy [6]. Scientists have been looking for ways to circumvent this limitation and boost the phase transition process.

One of the methods involves embedding the PCMs into solid porous foams; using metal foam (MF) improves the TES system efficiency [7–9]. Yang et al. [10] investigated the role of MF in enhancing heat transfer. Using MF instead of a PCM light pipe, the melting time was reduced by 88.55 percent. A comparative study by Abishek et al. [11] determined the melting time of pure PCM and PCM integrated with aluminum foam. By adding MF to the PCM, the melting rate decreased significantly. Nie et al. [12] evaluated the effect of foam made of copper on the paraffin thermal cycle. MF improved the heat transfer of PCM and sped up phase changes. Several thin-film MFPCM systems for cooling electronic components, such as processors, laptops, displays, and tablets, have recently been created [13]. MFPCMs were employed by Dede and Joshi [14] to construct battery cells that generate more power while running at a lower temperature. This idea can boost energy generation while also increasing battery life. Zhang et al. [15] investigated the effects of foam made of copper on the phase change of paraffin. The total melting time is reduced by 20.5% by adding the MF. Using foams made of copper and aluminum, Prasanth et al. [16] studied the melting performance of PCM. They concluded that there was no significant difference between the PCM melting times of aluminum foam and copper and that their extraction heat rates were also close to each other.

Another method is to disperse metallic nanoparticles (NPs) within PCMs to produce nanoparticle-enhanced PCMs (NPCMs) [17]. Nanoparticles have already been extensively used for improving the heat transfer of liquids in the form of nanofluids [18,19] or hybrid nanofluids [20]. NPs can improve the conductivity of PCMs and change their properties [21]. Nonetheless, several studies [22] have demonstrated that highly thermally conductive contents enhance the viscosity and conduction of NPCMs while reducing heat convection. Loading NPs can only improve the performance of TES systems at a specific concentration. An experimental study by Li et al. [23] established the synergistic effects of a fin and NPCM on a TES unit's performance and suggested a model to estimate the efficiency [24]. The study demonstrated that NPs enhance the performance of TES compared to clean PCM. Recently, Ho et al. [25] reported that NPs in working fluids have lower thermal resistance than nano-encapsulated PCM.

Recently, several studies have been published on how fins influence energy transmission in PCM-filled enclosures. Ji et al. [26] performed a numerical simulation of PCM melting in a hollow with a metal double-finned heat sink. Increasing the length of the lower fin and reducing the size of the upper fin have been found to improve PCM melting. Jmal and Baccar [27] found that many fins tend to lead to PCM confinement. The number of fins should be appropriate for each system. Abdi et al. [28] computationally studied the phase-change performance of a PCM in a TES unit with aluminum fins and without them. It has been found that longer fins transmit energy more efficiently than a large number of fins. Yazici et al. [29] studied the melting of PCM in a finned chamber by varying the chamber's inclination and the number of fins. The results indicated that the number of fins and the chamber angle significantly affect the system's operation time. Nakhchi and Esfahani [30] investigated the fin shapes of a heat sink. It has been demonstrated that the structure of the fins influences the melting of PCMs.

Guo et al. [31] designed a series of comparison experiments to shed light on the influence of MF and fins on heat transfer. Each MF and fin caused a boost in the phase-change rate of PCMs, but multiple MF and fin combinations had the most significant impact. Zhang et al. [32] examined three popular ways to improve a TES unit's performance in a simulation study. These include heat pipes, foam made of copper, and fins. Combining heat pipes and MF improved the melting rate, but combining fins and heat pipes yielded the best solidification results. Joshi et al. [33] also studied the influence of MF and fins on heat transfer performance. While the utilization of MF increased both the solidification and melting rates by 33.33% and 16.67%, fin use increased both by 5.56% and 50%. A study conducted by Senobar et al. [34] examined the effects of PCM, MF, and NPs in combination. Hybrids, in all ways, improved the phase change rate by 24% compared with the pure PCM.

Sheikholeslami et al. [35] designed a TES unit with triangular fins and CuO nanoparticles to study the phase-changing abilities. A reduction in discharging and melting occurs due to the presence of NPs. With triangular fins, solidification rates improve by 40.75%, while with NPs, rates decline by 44.88%. Using a tank with fins, Kok [36] measured NP–PCM charging in a tank with fins and concluded that an increasing number of fins would boost TES performance and decrease melt time. Pássaro et al. [37] examined the effect of fins and the combination of NPs and fins on a TES unit's melting and outlet temperatures. As a result, adding graphene NPs significantly improved the thermal conductivity, and combining NPs and fins enhanced discharge performance.

In the literature design, the PCM is typically confined in an enclosure where the heat transfer occurs at the enclosure surface. The present TES design allows a flow of liquid PCM into the enclosure to further enhance the heat transfer and boost the heat transfer rate by direct contact between heated liquid and solid PCM. Here, the dynamic melting of an NPCM stream in a shell-tube open TES system enhanced with fin and metal foam was modeled and analyzed for the first time. The copper fin, copper metal foam, and CuO–coconut oil as heat transfer enhancers were applied to further increase the heat transfer.

2. Model Description and Mathematical Formulation

2.1. Model Description

Fast-charging low-temperature industrial waste heat (IWH) recovery demands quick and efficient thermal energy storage in a compact space. Thus, latent-heat phase-change materials represent an ideal solution. However, their low thermal conductivity is a barrier to their practical usage in IWH. Here, we propose a new latent-heat thermal energy storage design, which benefits from a stream of liquid PCM. Figure 1 shows a view of an open latent-heat thermal energy storage (LHTES) unit loaded with copper foam saturated by a nano-enhanced phase-change material (NPCM). The NPCM is made of CuO–coconut oil, which is embedded in the copper foam. The inner wall of the chamber is kept at a uniform hot temperature, Th. Furthermore, a hot NPCM liquid at a uniform temperature, Th, enters the chamber from below at a static gauge pressure, Pin, and exits from the top with a zero-gauge pressure. The NPCM inside the chamber is initially in a sub-cold solid state. Hot NPCM is pressurized at the chamber's inlet to thermally charge the chamber, while the inner tube is also maintained at the hot temperature, Th. A fin is attached to the hot wall to divert the hot NPCM liquid toward solid regions.

Initially, a flow of NPCM from the chamber's inlet to the outlet is not feasible since all of the NPCM is solid. After a sufficient time, some of the NPCM inside the chamber is melted in the areas adjacent to the hot inner tube, and a thin liquid film forms around the inner tube, allowing a flow of hot PCM from the bottom inlet toward the top outlet.

The modeling assumption is as follows: (I) NPCM is an incompressible fluid, and it enters and leaves the chamber continuously. (II) At all times, a local thermal equilibrium (LTE) is established between the phase-change material and the porous solid matrix. (III) The copper foam is a porous medium with a uniform structure and constant porosity and permeability. (IV) The natural convection was taken into account using the Boussinesq model. Considering the above assumptions, the governing equations for the control of mass, momentum, and energy in the chamber are explained.

2.2. Mathematical Formulation

The control equations for the flow and heat transfer of NPCM in metal foam [38–40]:

$$\frac{1}{r}\frac{\partial(ru)}{\partial r} + \frac{\partial w}{\partial z} = 0 \tag{1}$$

$$\frac{\rho_{\mathrm{NPCM}}}{\varepsilon}\frac{\partial u}{\partial t} + \frac{\rho_{\mathrm{NPCM}}}{\varepsilon^2}\left(u\frac{\partial u}{\partial r} + w\frac{\partial u}{\partial z}\right) = -\frac{\partial P}{\partial r} + \frac{\mu_{\mathrm{NPCM}}}{\varepsilon}\left(\frac{1}{r}\frac{\partial}{\partial r}\left(r\frac{\partial u}{\partial r}\right) - \frac{u}{r^2} + \frac{\partial^2 u}{\partial z^2}\right) - \frac{\mu_{\mathrm{NPCM}}}{K}u - s(T)u \tag{2}$$

$$\frac{\rho_{\mathrm{NPCM}}}{\varepsilon}\frac{\partial w}{\partial t}+\frac{\rho_{\mathrm{NPCM}}}{\varepsilon^2}\left(u\frac{\partial w}{\partial r}+w\frac{\partial w}{\partial z}\right)=-\frac{\partial P}{\partial z}+\frac{\mu_{\mathrm{NPCM}}}{\varepsilon}\left(\frac{1}{r}\frac{\partial}{\partial r}\left(r\frac{\partial w}{\partial r}\right)+\frac{\partial^2 w}{\partial z^2}\right)$$
$$-\frac{\mu_{\mathrm{NPCM}}}{K}w-s(T)w+\rho_{\mathrm{NPCM}}g\beta_{\mathrm{NPCM}}\left(T-T_f\right) \quad (3)$$

$$(\rho c_p)_{\mathrm{composite}}\frac{\partial T}{\partial t}+(\rho c_p)_{\mathrm{NPCM,l}}\left(u\frac{\partial T}{\partial r}+w\frac{\partial T}{\partial z}\right)+\varepsilon\rho_{\mathrm{NPCM,l}}L_f\frac{\partial\phi(T)}{\partial t}$$
$$=\left(\frac{1}{r}\frac{\partial}{\partial r}\left(k_{\mathrm{composite}}\frac{\partial T}{\partial r}\right)+\frac{\partial^2 T}{\partial z^2}\right) \quad (4)$$

and

$$s(T)=A_{mush}\frac{1-2\phi+\phi^2}{\lambda+\phi^3} \quad (5)$$

in which ϕ is a function of temperature introduced as:

$$\phi(T)=\begin{cases}0 & T<T_{fusion}-\Delta T_{fusion}/2\\ \frac{T-T_{fusion}}{\Delta T_{fusion}}+\frac{1}{2} & T_{fusion}-\Delta T_{fusion}/2<T<T_{fusion}+\Delta T_{fusion}/2\\ 1 & T>T_{fusion}+\Delta T_{fusion}/2\end{cases} \quad (6)$$

where T_{fusion} is the fusion temperature, and ΔT_{fusion} is the melting temperature range. The dynamic viscosity was considered as $\mu_{\mathrm{PCM}}=\phi\mu_{\mathrm{NPCM,l}}+(1-\phi)\times\mu_{\mathrm{NPCM,s}}$ to improve the stability and accuracy of the solution. Here, $\mu_{\mathrm{NPCM,s}}$ is not physically meaningful. However, since the velocity in the solid region should approach zero, a large value of artificial viscosity in a solid region contributes to the stability and accuracy of the solution. Thus, a large value of $\mu_{\mathrm{NPCM,s}}$ = 1000 Pa s was adopted here. Moreover, the derivatives of μ_{NPCM} in the momentum equation were neglected since the only aim of variable viscosity is to help the velocity reach zero in the solid region. Furthermore, L_f denotes the latent heat of NPCM. A_{mush} is a large value, and λ is a small value, which forces the velocity to zero in solid regions. In clear flow studies, A_{mush} is typically in the order of 10^6 Pa·s·m^{-2}, but since the hydrodynamic resistance in porous media is large, A_{mush} should also be adapted with a higher value. In the present study, A_{mush} and λ were adopted as 1×10^{10} Pa·s·m^{-2} and 0.001, respectively.

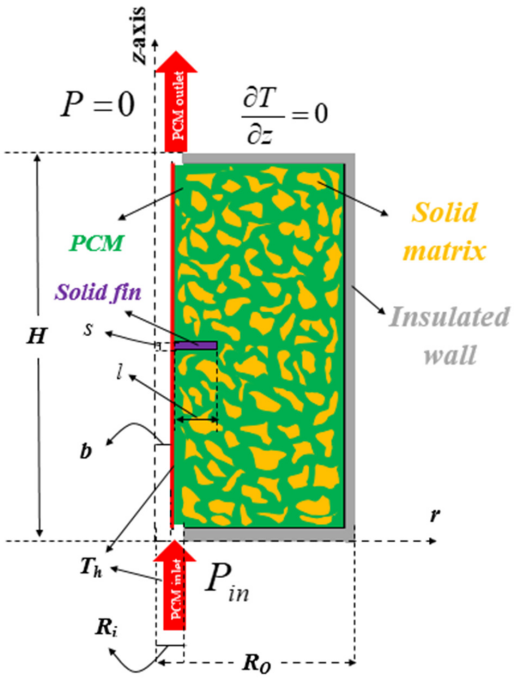

Figure 1. Schematic diagram of an open latent-heat thermal energy storage unit for fast-charging low-temperature heat recovery.

The metal foam permeability is computed using the following relation [41,42]:

$$\begin{aligned} K &= d_p^2 \frac{73\times10^{-5}}{(1-\varepsilon)^{0.224}} \left(d_l d_p^{-1}\right)^{-1.11}, \\ \left(d_l d_p^{-1}\right) &= 1.18\left(\frac{1-\varepsilon}{3\pi}\right)^{0.5}[1-\exp(-(1-\varepsilon)/0.04)]^{-1}, d_p = 254\times10^{-4}/\iota \end{aligned} \tag{7}$$

where ι is the foam's pore density and is equal to 5 PPI. The effective thermophysical properties of PCM and composite metal foam are evaluated as a weight average property for the metal foam and PCM using the porosity (ε), as:

$$k_{\text{composite}} = \varepsilon k_{\text{NPCM}} + (1-\varepsilon)k_{\text{mf}} \tag{8}$$

where the subscript of mf denotes the metal foam, and the subscript of composite indicates the effective thermophysical properties of the metal foam and PCM inside the pores. Similarly, the effective heat capacity is evaluated as:

$$\left(\rho c_p\right)_{\text{composite}} = \varepsilon\left(\rho c_p\right)_{\text{NPCM}} + (1-\varepsilon)\left(\rho c_p\right)_{\text{mf}} \tag{9}$$

The thermophysical properties of PCM are a function of liquid fraction, as:

$$k_{\text{NPCM}} = \phi k_{\text{NPCM},l} + (1-\phi)k_{\text{NPCM},s} \tag{10}$$

$$\left(\rho c_p\right)_{\text{NPCM}} = \phi\left(\rho c_p\right)_{\text{NPCM,l}} + (1-\phi)\left(\rho c_p\right)_{\text{NPCM,s}} \tag{11}$$

The thermophysical properties of NPCM were also computed as:

$$\left(\rho C_p\right)_{\text{NPCM}} = (1-\gamma)\left(\rho C_p\right)_{\text{NPCM}} + \gamma\left(\rho C_p\right)_{np} \tag{12a}$$

$$\rho_{\text{NPCM}} = (1-\gamma)\rho_{\text{NPCM}} + \gamma\rho_{np} \tag{12b}$$

$$\frac{k_{\text{NPCM}}}{k_{\text{PCM}}} = \frac{k_{\text{np}} + 2k_{\text{PCM}} - 2\gamma\left(k_{\text{PCM}} - k_{\text{np}}\right)}{k_{\text{np}} + 2k_{\text{PCM}} + \gamma\left(k_{\text{PCM}} - k_{\text{np}}\right)} \tag{12c}$$

$$\frac{\mu_{\text{NPCM}}}{\mu_{\text{PCM}}} = \frac{1}{(1-\gamma)^{2.5}} \tag{12d}$$

$$L_f = (1-\gamma)L_{f,PCM} \tag{12e}$$

In the above, substituting the thermophysical properties of solid and liquid PCM gives the thermophysical properties of solid and liquid NPCM, respectively. In Equation (12e), the latent heat was estimated as the latent heat of the PCM part only, since the nanoparticles do not experience a phase change during the energy storage process. Here, $L_{f,PCM}$ shows the latent heat of PCM. Moreover, the energy conservation equation for the solid horizontal fin as an obstacle is given by [40,43]:

$$\left(\rho c_p\right)_{fin}\frac{\partial T}{\partial t} = k_{fin}\left(\frac{1}{r}\frac{\partial}{\partial r}\left(\frac{\partial T}{\partial r}\right) + \frac{\partial^2 T}{\partial z^2}\right) \tag{13}$$

2.3. Boundary Conditions

The related boundary conditions for the proposed geometry, Figure 1, can be written as follows:

The PCM enters the enclosure due to high gauge pressure, P_{in}, with a hot temperature, T_h:

$$P = P_{in} \text{ and } T = T_h \tag{14}$$

and it leaves the enclosure at zero gauge pressure:

$$u = 0,\ P = 0,\ \text{and}\ \frac{\partial T}{\partial z} = 0 \tag{15}$$

The perimeter top, bottom, and vertical walls of the enclosure are well-insulated with no-slip and no-permeability boundary conditions, as:

$$u = w = 0,\ \frac{\partial T}{\partial n} = 0 \tag{16}$$

where n is the surface normal vector. The domain is initially at a cold temperature of $T_{initial}$ and zero velocity and pressure:

$$v = w = 0,\ p = 0,\ T = T_{initial} \tag{17}$$

For the interface of fin and composite, the no-slip and no-permeability were applied. Considering the heat equation, the continuity of temperature and heat flux between the composite PCM and fin was employed. Hence, the fin-composite boundary conditions can be explained as:

$$v = w = 0,\ T_{composite} = T_{fin},\ k_{composite}\frac{\partial T_{composite}}{\partial n} = k_{fin}\frac{\partial T_{fin}}{\partial n} \tag{18}$$

2.4. Total Energy Stored in the Unit (ES) and Melting Volume Fraction (MVF)

The stored energy is the combination of sensible and latent heat and is computed using volume integration over the axis-symmetric domain as:

$$ES(t) = \overbrace{\int_V \left(\int_{T_{initial}}^{T} (\rho c_p)_{composite} dT\right) dV}^{Sensible\ Energy\ Stored} + \overbrace{\int_V \left(\varepsilon \rho_{\mathrm{PCM},l} L_f\right) \phi dV}^{Latent\ Energy\ Stored} \tag{19}$$

where V is the volume of the enclosure. The normal liquid volume fraction, the average liquid portion, is evaluated by normalizing the amount of liquid PCM with respect to the total void volume of the enclosure, as:

$$MVF(t) = \frac{\int_V \varepsilon \phi(T) dV}{\int_V \varepsilon dV} \tag{20}$$

The outlet flow rate, average outlet velocity, and average outlet temperature are computed as:

$$\mathrm{Flowrate}(t) = 2\pi \int_b^{R_i} w(r) r dr \tag{21}$$

$$w_{avg}(t) = \frac{\mathrm{Flowrate}(t)}{2\pi \int_b^{R_i} r dr} \tag{22}$$

$$T_{avg}(t) = \frac{\int_b^{R_i} T(t) w(t) r dr}{w_{avg}(t)} \tag{23}$$

where 2π is entered into the equations since the model is axis-symmetric.

Coconut oil with a low fusion temperature of 24 °C was selected as a PCM embedded in a copper foam. The thermophysical properties of the PCM and foam are shown in Table 1.

In the current research, $T_{initial}$ = 15 °C, T_h = 60 °C, b = 3/8″ (9.53 mm), H = 16″ (406.40 mm), s = 1/4″ (6.35 mm), R_i = 7/8″ (22.23 mm), and R_o = 8″ (203.20 mm) were considered fixed. Thus, the PCM is initially in a super cold condition. Using these data, the inlet and outlet lengths can be computed as (R_i-b) = 1/2″ (12.70 mm). The inlet pressure (P_{in}), fin length (l), and porosity (ε) are alterable, and their impact on the thermal charging behavior of the enclosure is investigated in the results and discussion section. The typical values of alterable parameters were taken as P_{in} = 3000 Pa, l = 1.6″ (40.64 mm), and ε = 0.95. The results will be reported for these typical values; otherwise, the parameter values will be stated.

Table 1. Thermophysical properties of the coconut oil and the nano-additives [44,45].

Properties	Coconut Oil (Measured)		Copper Fin	Copper Foam
	Solid (15 °C)	Liquid (32 °C)		
ρ (kg/m^3)	920	914 ± 0.11%	8900	8900
μ (kg/m s)	-	0.0326 ± 3%	-	-
C_p (J/kg K)	3750	2010 ± 0.2%	386	386
k (W/m K)	0.228	0.166 ± 1.2%	380	380
h_f (kJ/kg)	-	103 ± 1%	-	-
Pr	-	394.73 ± 3.2%	-	-
T_{fusion} (°C)	24	-	-	-

3. Numerical Method and Model Verification

3.1. Numerical Approach

Following the standard finite element method procedure, the control equations in the porous domain and solid fin, along with corresponding boundary conditions, were transformed into weak equations. The equations were integrated over unstructured mesh elements to obtain a set of algebraic residual equations. Then, the Newton method based on The PARDISO solver [46,47] was employed to solve the algebraic equations for pressure, velocity components, and temperatures in a coupled way. The solver stops the computations once the melting volume fraction in the thermal energy storage unit reaches a value below 0.999, indicating that the NPCM is fully melted. A backward differential formula [41] was also invoked to automatically control solver steps and fix the relative error below 10^{-4} for all variables. The solver steps are explained in Figure 2. The mesh study and verifications were carried out, and the details are reported in the next section.

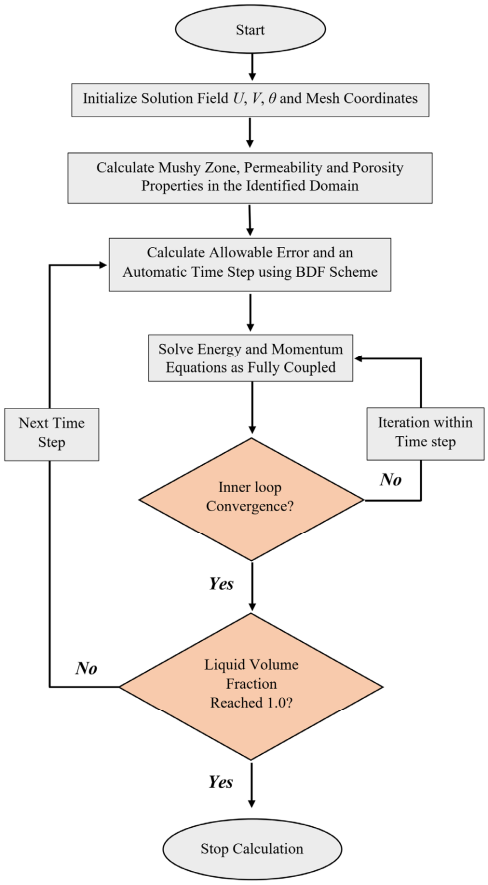

Figure 2. Diagram of the numerical method and the solver steps.

3.2. Grid Independency Process

The influence of the mesh size on the accuracy of computations is surveyed by repeating the computations for several mesh sizes. The case ε = 0.95, P_{in} = 3000 Pa, and γ = 0 was adopted as a reference case, and the results of the mesh study are reported for this configuration. The details of selected mesh sizes and the corresponding computational time are summarized in Table 2. The variation in NPCM average velocity, MVF, energy storage, and outlet flow rate is depicted in Figure 3. The data for case VI was not plotted in some of the figures since they closely overlapped with cases IV and V. It can be seen that the results are sensitive to mesh size. This can be due to the thermal behavior of the unit and the initiation of the initial liquid layer over the heated tube, which allows a liquid stream into the enclosure. The findings indicate that using a mesh size smaller than case IV provides an acceptable accuracy almost independent of the mesh size. The average outlet velocity and flow rate are the variables most sensitive to the mesh size. The reason is that the outlet is comparatively small, and a coarse mesh can cover the outlet region with only a few elements. Hence, a fine mesh is required to adequately capture the flow gradients at the enclosure inlet and outlets. Thus, the mesh case IV was adopted for all computations of the current research. Figure 4 shows an overview and detailed sections of the utilized mesh. This figure shows that the adopted mesh provided a fine element distribution at the enclosure outlet.

Table 2. Details of selected meshes for the mesh study.

Cases	Number of Elements		Results at 750 s		Computational Time
	NPCM Domain	Fin Domain	MVF	Stored Energy (kJ/kg)	
Case I	3488	65	0.8162	6.0893	17 min
Case II	5910	106	0.8403	6.2862	25 min
Case III	13,846	250	0.8611	6.4531	49 min
Case IV	33,796	761	0.8788	6.5927	6 h 34 min
Case V	55,520	827	0.8764	6.5724	12 h 29 min
Case VI	75,200	1050	0.8763	6.5720	24 h 32 min

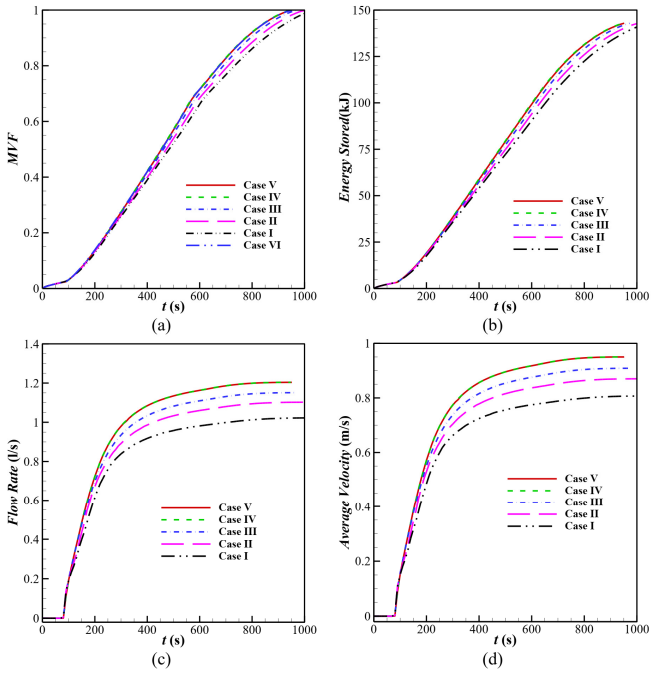

Figure 3. Impact of mesh size on the accuracy of the results. (**a**) MVF, (**b**) energy storage, (**c**) outlet flow rate, (**d**) NPCM average velocity.

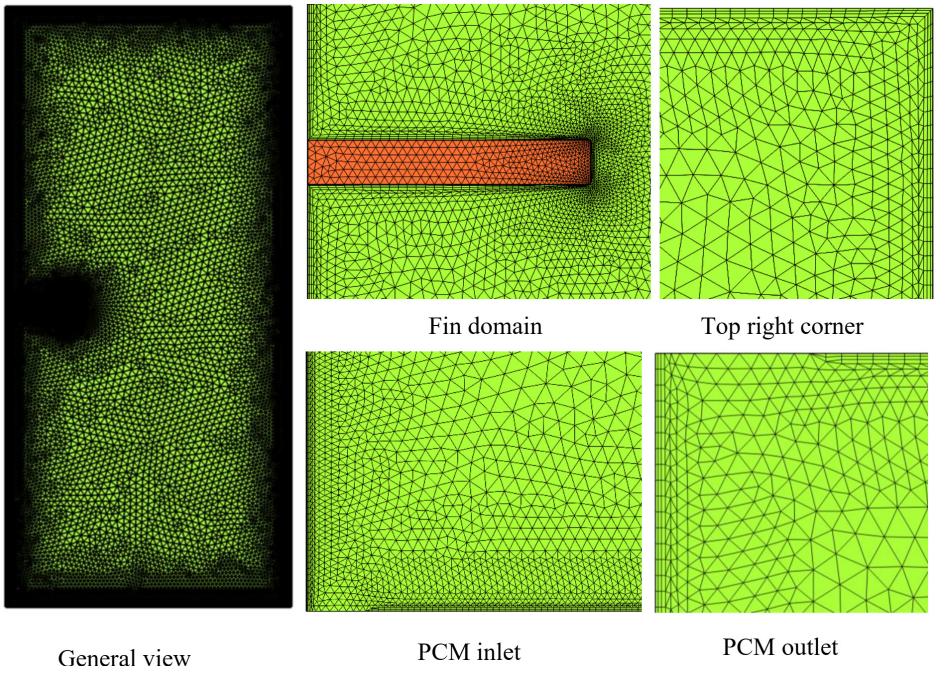

Figure 4. A detailed view of the selected mesh (case IV).

3.3. Validation

The accuracy of the current numerical model and simulations was tested against Kamkari et al.'s experimental study [48]. These authors investigated the thermal charging of lauric acid in a chamber of size 0.12 × 0.05 m isothermally heated from the left sidewall. Figure 5 illustrates the measured stored energy during the thermal charging measured by [48] and the simulated data of the current research. A fair agreement between the studies can be observed. Furthermore, the present model was also verified against the data of Zheng et al. [15] and Al-Jethelah et al. [44] for the thermal charging of phase-change material in foams and was found to be in good agreement. For the sake of brevity, the graphs are not reported here.

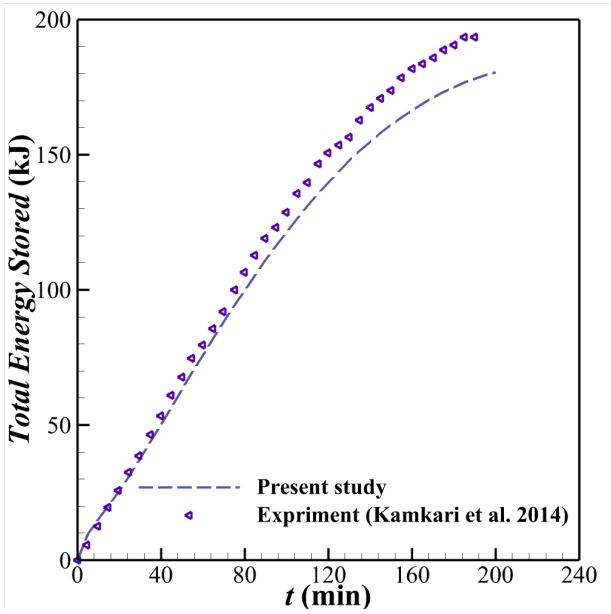

Figure 5. Measured stored energy in the enclosure during melting by [48] against the simulated data of the current study.

4. Results and Discussion

The parameters of interest are the metal foam porosity, the inlet pressure, the fin's length, and the nanoparticle concentration. Table 3 shows the values adopted for the first three parameters. The influence of the nanoparticle concentration on thermal energy storage was also addressed for the γ in the range of 0–0.05. The results are reported in graphs for liquid volume fraction (MVF), amount of stored energy, flow rate, and average outlet temperature. Moreover, the streamlines and isotherms are plotted to analyze the melting process.

Table 3. The range and level of control parameters.

Parameter	Level 1	Level 2	Level 3	Level 4
ε Porosity	0.85	0.90	0.95	0.975
P_{in} Pressure inlet (Pa)	500	1000	2000	4000
L_{fin} Length of fin * (mm)	13 (0.5″)	25 (1″)	41 (1.6″)	50 (2″)

* Case L_{fin} = 1mm (0.03″) was also computed, which can be considered a case with no fin.

Figure 6 shows the impact of the porosity on the melting fraction, the amount of energy stored, the flow rate, and the average temperature of the chamber's outlet at a given time. A slope change in the curves of Figure 6a can be observed. This slope change corresponds to the creation of a liquid NPCM in the vicinity of the heated tube. The liquid NPCM allows a passage between the inlet, where the hot NPCM enters the chamber, and the outlet. Therefore, the slope's change indicates the activation of the forced convection mechanism due to the flow of hot liquid NPCM into the chamber. The slope's change occurs for all porosities almost at the same time.

Entering the hot NPCM into the chamber creates a mixed convection flow and accelerates the melting process of the NPCM inside the chamber. Moreover, the time required to complete the melting process was extended by increasing the porosity. The fastest melting occurred for the minimum value of the porosity (ε = 0.85) and was about 11 min (685 s). Increasing the porosity from 0.85 to 0.9 added about one minute (67 s) to the melting process. In most studies from the literature, the typical thermal charging time is more than seven hours. Thus, the dynamic melting in metal foams provides a fast-charging mechanism.

Moreover, increasing the porosity from ε = 0.85 to 0.95 increases the charging time from 11 min to 15 min. Thus, a 0.1 change in porosity adds 4 min to the required charging time. Finally, the time difference is about 10 min (598 s) for the phase-change material to melt completely at ε = 0.975 compared to that of ε = 0.85. Therefore, the time required to complete the melting process of NPCM increases almost logarithmically by raising the porosity coefficient. An increase in porosity reduces the share of the porous solid matrix. It increases the void space, which, as a result, weakens the thermal conductivity of composite NPCM metal foam and, consequently, the conduction heat transfer mode. However, a metal foam with a high porosity imposes a low flow resistance and enhances the convection heat transfer mode.

As seen in Figure 6b, an increase in the porosity increases the stored heat since a foam with high porosity can hold more NPCM. It should be noted that copper foam does not contribute to phase change and cannot store latent thermal energy. Moreover, it should be noted that the simulation stops as soon as the MVF reaches unity (0.999), indicating full latent-heat thermal charging.

As is clear, the capacity to store energy increases over time through almost the same slope for all four curves, while the amount of stored energy is elevated at higher porosity values. Hence, here, thermal charging power can be introduced as the amount of stored energy divided by the required time for full thermal charging (full melting). For the lowest to the highest values for the porosity (ε = 0.85 to ε = 0.975), the thermal charging power per unit of weight was obtained as 12.6 kW/kg, 14.3 kW/kg, 15.1 kW/kg, and 13.2 kW/kg,

respectively. Hence, shifting the heat transfer mode from conduction to mixed convection by increasing the porosity leads to the optimum value for stored energy. The optimal value for maximizing storage capacity is associated with $\varepsilon = 0.95$, followed by $\varepsilon = 0.9$ and $\varepsilon = 0.975$, while the lowest thermal charging power corresponds to the lowest value for the porosity, $\varepsilon = 0.85$.

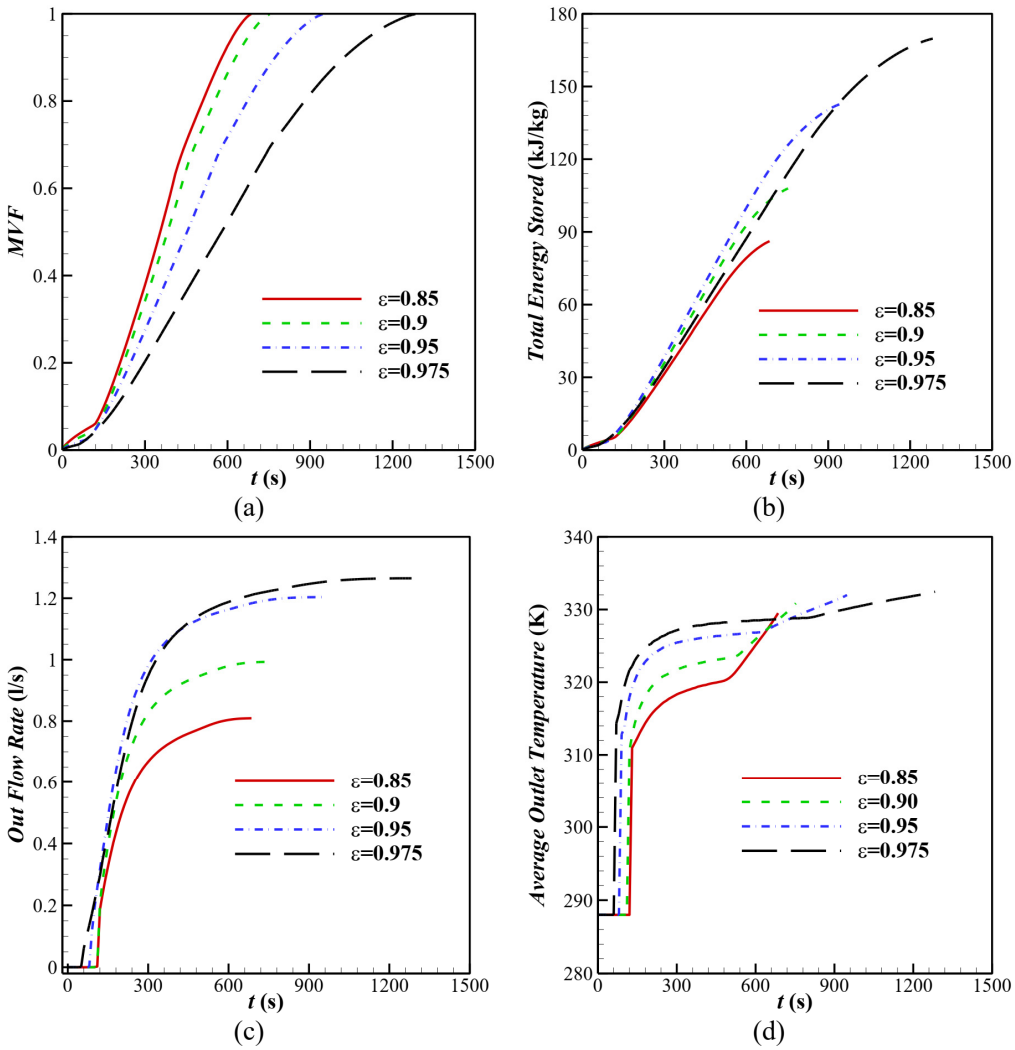

Figure 6. Effect of porosity parameter (ε) on (**a**) melting volume fraction, (**b**) total energy stored, (**c**) outlet flow rate, and (**d**) average outlet temperature in the time range of zero up to 1500 s.

A porosity of $\varepsilon = 0.95$ provides a melting time of about 15 min, while a porosity of $\varepsilon = 0.975$ corresponds to a 20 min melting time. A porosity of $\varepsilon = 0.95$ can provide fair energy storage since it theoretically reduces the volume capacity of the chamber only by 2.5% compared to case $\varepsilon = 0.975$ while reducing the thermal storage time by 25% compared to case $\varepsilon = 0.975$.

The effect of the porosity coefficient on the outlet flow rate of the chamber is shown in Figure 6c. As explained, when the liquid NPCM allows for flowing in the chamber, the slope of the curves sharply increases. This figure confirms that the highest flow rate occurred for the highest porosity value. As mentioned, with raising the porosity coefficient, the share of porous solid matrix decreases, so the permeability of the foam increases and the foam's resistance to liquid PCM flow decreases.

Interestingly, the outlet flow for the highest porosity value ($\varepsilon = 0.975$) was raised by more than 56% compared to the lowest value ($\varepsilon = 0.85$). The outlet flow rate from the chamber for other porosity values, i.e., 0.9 and 0.95, were respectively increased by 23 and

49% compared to the output flow corresponding to the lowest porosity value ($\varepsilon = 0.85$). It is worth mentioning that a high flow rate at the outlet leads to a higher inlet flow rate to replace the molten NPCM and increases the strength of the convective heat transfer.

Figure 6d depicts the average outlet temperature from the chamber. It can be seen that in the very first moments, the average outlet temperature of the NPCM suddenly increases and then declines with a gentle slope. The difference in temperature between the phase-change material and the hot wall is the highest. Therefore, in the initial moments, the highest thermal gradient occurs between the phase-change material and the hot wall, and the temperature of the NPCM increases sharply. Over time, the NPCM and the hot wall will gradually reach an equilibrium at a hot temperature. So, the temperature for all four curves with a gentle slope will reach the boundary condition temperature, T_h, which is slightly higher than 330 K.

The effects of the porosity on the isotherms and streamlines at the selected instances of 300 s, 600 s, and 900 s are shown in Figures 7 and 8. Here, the minimum and maximum values of the porosity were adopted for investigation. As seen, for the minimum porosity ($\varepsilon = 0.85$) and particularly at the initial time, there is a noticeable distance between isotherms due to the well-improved thermal conductivity. Over time, as the melting front progresses, the isotherms are compacted to the right top corner of the chamber, where most NPCM remains in the solid state. On the other hand, over time, it can be observed that the isotherms are fairly distributed around the melting interface when $\varepsilon = 0.85$, indicating moderate temperature gradients. When porosity increases, the temperature gradient rises at the melting interface and compacts the isotherms. This observation is because of the difference between the NPCM-composite thermal conductivities of these two cases.

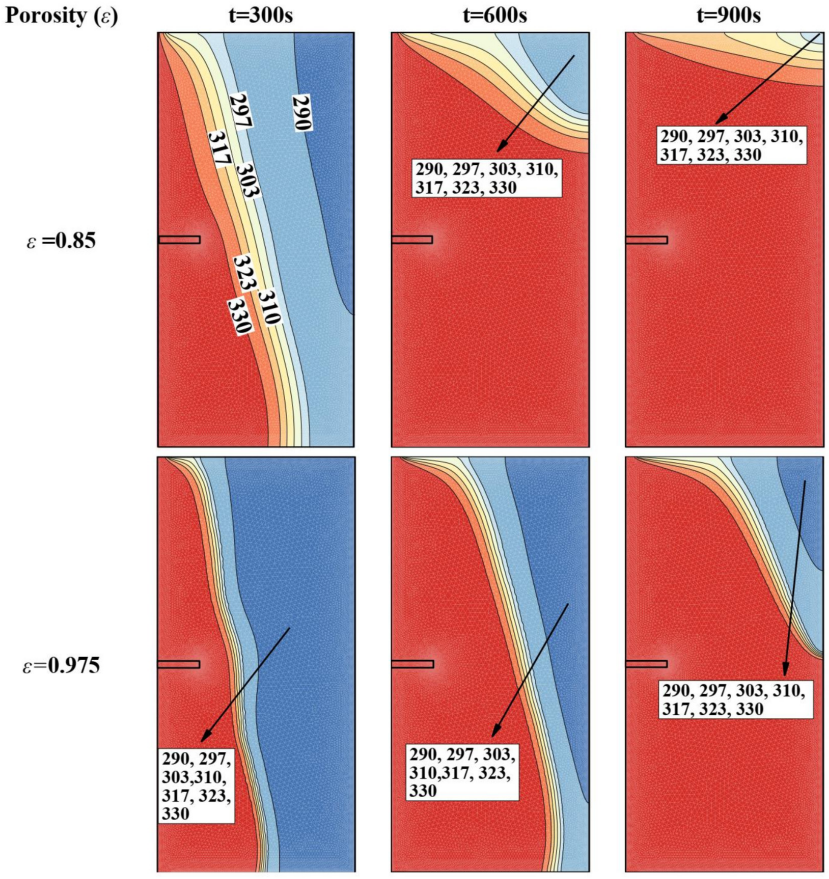

Figure 7. Effect of the porosity parameter on the contours of the isotherm (K): (**top row**) $\varepsilon = 0.85$ and (**bottom row**) $\varepsilon = 0.975$.

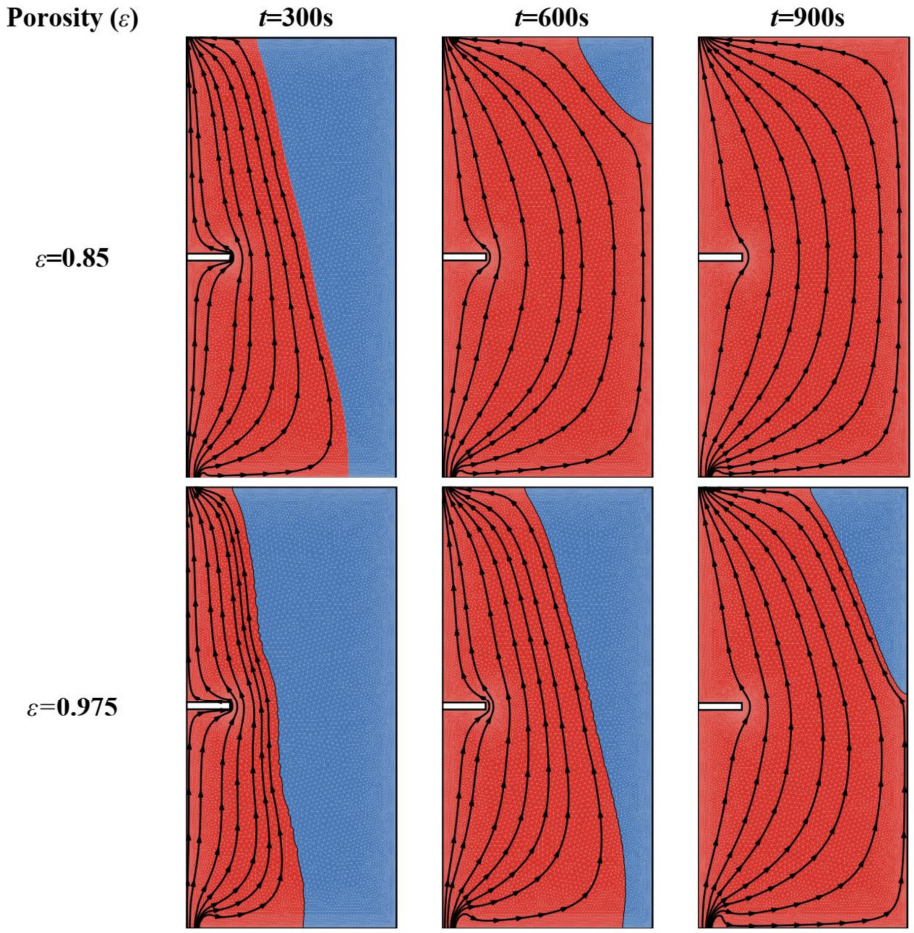

Figure 8. Effect of the porosity parameter on the streamlines: (**top row**) $\varepsilon = 0.85$ and (**bottom row**) $\varepsilon = 0.975$.

It should be noted that although the increase in thermal conductivity reduces the temperature gradients, the overall heat transfer is the multiplication of effective thermal conductivity and the temperature gradient. Thus, the overall conduction heat transfer is expected to increase as the porosity decreases. However, here, the mixed convection heat transfer and hydrodynamics of the molten NPCM, as well as the effective latent-heat capacity, play an essential role in the thermal charging time of the chamber.

Figure 8 shows that the streamlines are fairly distributed next to the melting front in the case of $\varepsilon = 0.85$, while they are close to each other when $\varepsilon = 0.975$. The difference is due to the permeability of these two porous layers. Under a constant inlet pressure, a larger flow rate of liquid NPCM enters the chamber when the porosity is higher. Although in the case of $\varepsilon = 0.975$, the flow rate is higher than case $\varepsilon = 0.85$, which could be translated to better mixed-convection circulation and higher temperature gradients, the better effective thermal conductivity of case $\varepsilon = 0.85$ and the lower mass of NPCM inside the pores reduce the thermal charging time of the chamber.

Figure 9 exhibits the impact of the inlet pressure on the thermal characteristics of the chamber. Entering the liquid NPCM at a high pressure increases the overall flow rate and exit temperature and accelerates the thermal charging time of the chamber. Figure 9a shows that the higher the inlet static pressure, the higher the hydrodynamic driving force and the higher the liquid NPCM velocities. The melting times of 845 s (14 min), 1121 s (18.5 min), 1542 s (26 min), and 2183 s (36 min) correspond to inlet pressures of 4000 Pa, 2000 Pa, 1000 Pa, and 500 Pa, respectively. Therefore, it can be concluded that raising the inlet pressure by eight times reduces the melting time by about 22 min.

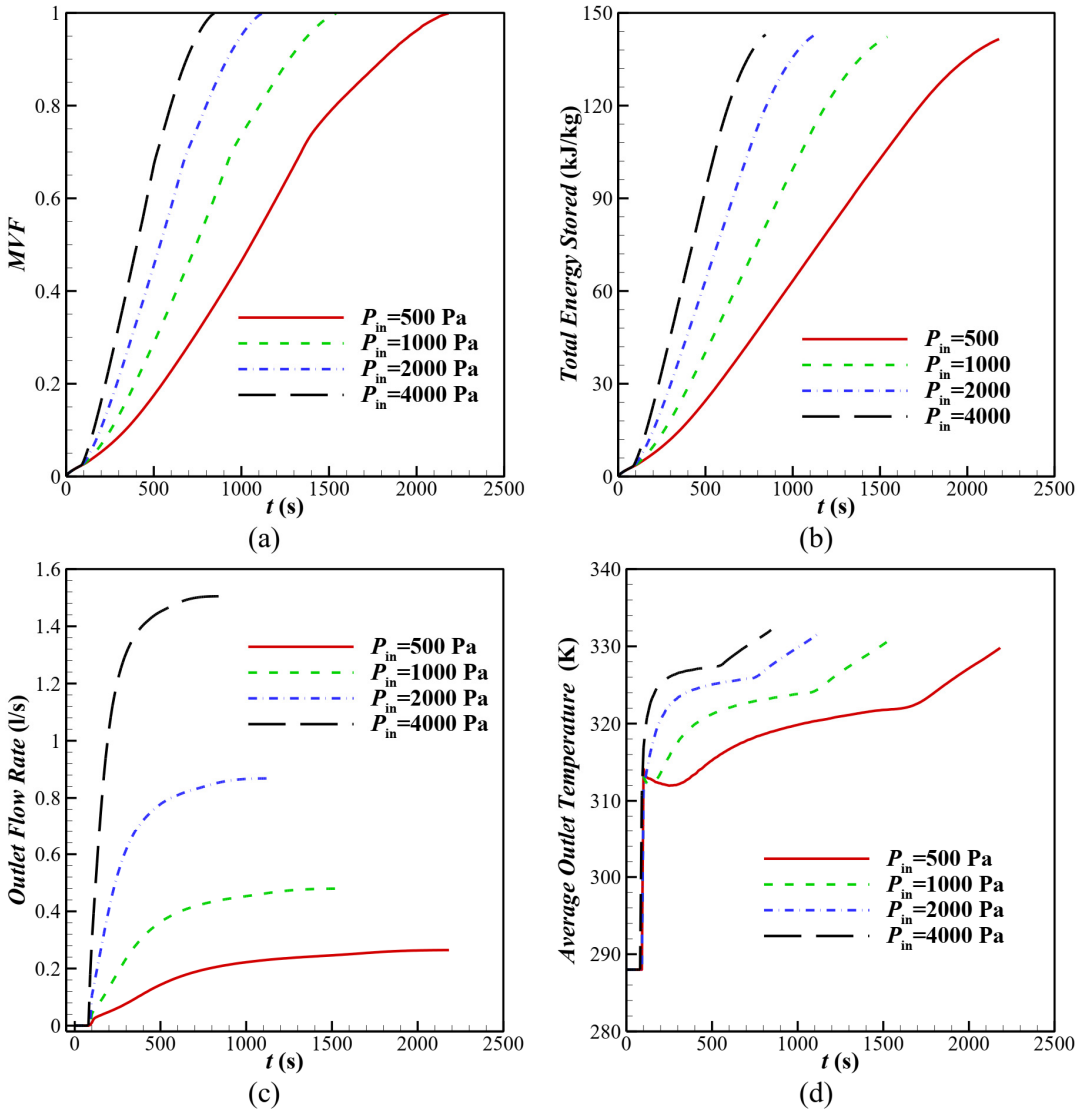

Figure 9. Effect of inlet pressure (P_{in}) on (**a**) melting volume fraction, (**b**) total energy stored, (**c**) outlet flow rate, and (**d**) average outlet.

As shown in Figure 9b, the amount of energy stored reaches its maximum value sooner by elevating the static pressure at the inlet. However, increasing the pressure does not affect the maximum amount of stored energy. Therefore, as mentioned before, there will be a time interval of 22 min to reach the maximum amount of stored energy between the maximum and minimum values of the inlet pressure. Hence, the energy storage power of 4000 Pa and 500 Pa inlet pressure is 17 kW/kg and 6.5 kW/kg, respectively. Thus, the studied cases could observe an eight-fold increase in inlet pressure resulting in a 2.6-fold increase in thermal charging power.

Raising the inlet pressure increases the flow rate of the liquid NPCM and increases the average outlet temperature during the melting process, as seen in Figure 9c,d. The highest (Q = 1.5 L/s) and lowest (Q = 0.26 L/s) flow rates correspond to the highest static pressure (P_{in} = 4000 Pa) and the lowest static pressure (P_{in} = 500 Pa), respectively. An eight-fold increase in the inlet pressure increases the flow rate by about 5.75 times.

The impact of the fin length on MVF, stored energy, flow rate, and average outlet temperature is shown in Figure 10. As can be seen in Figure 10a, as the fin's length increases to 41 mm, there is no noticeable change in the melting front. However, as the fin's length grows further, a steep slope occurs at later times, indicating the delayed arrival of the liquid

NPCM into the chamber, commencing forced convection heat transfer. Therefore, it can be seen that the length of 41 mm is the critical length value for the fin after that (L_{fin} = 50 mm). For any fin length longer than 41 mm, the increase in the charging times is noticeable.

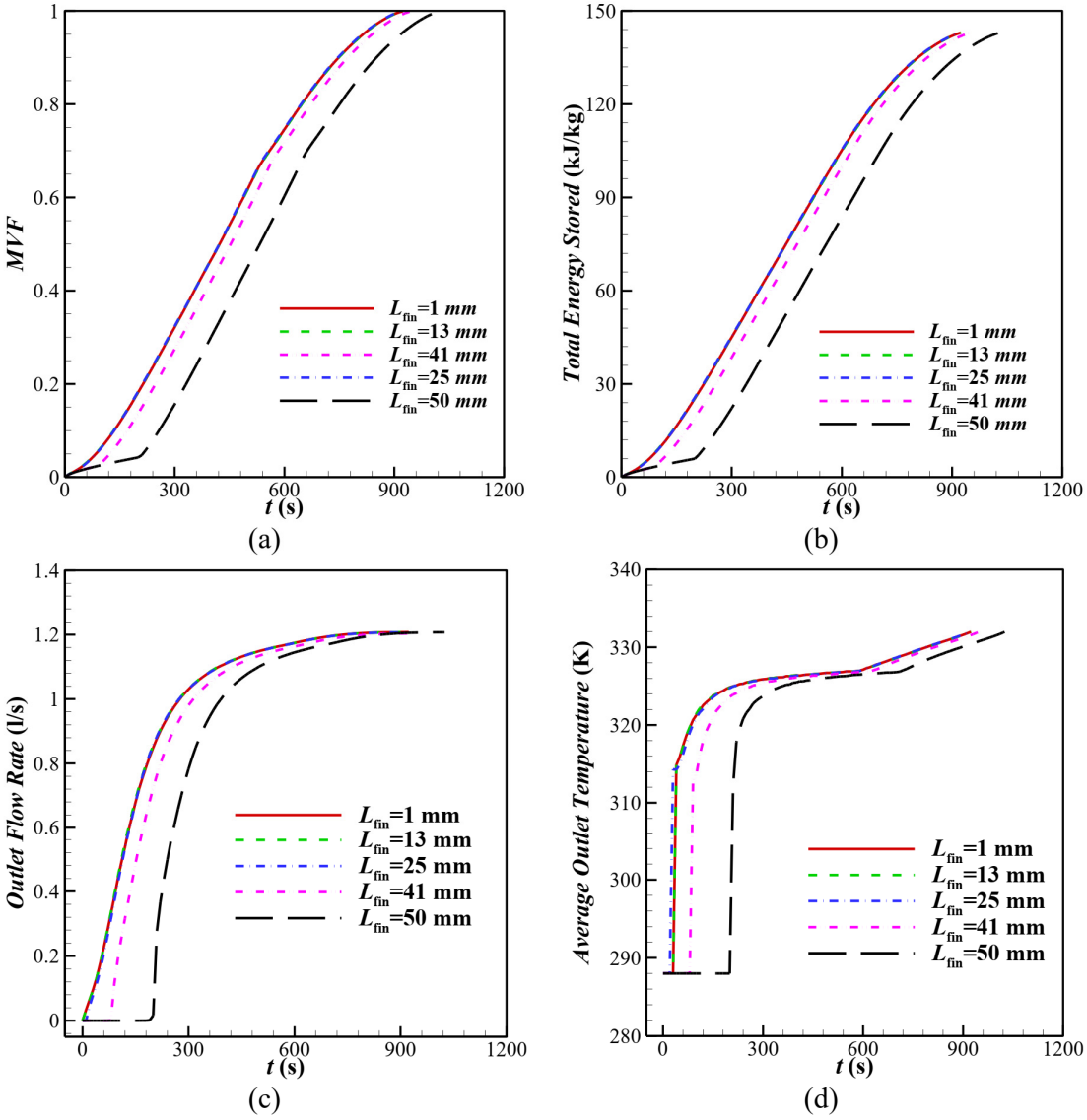

Figure 10. Effect of length of the fin (L_{fin}) on (**a**) melting volume fraction, (**b**) total energy stored, (**c**) outlet flow rate, and (**d**) average outlet temperature.

Forming a liquid NPCM film and opening a liquid passage between the inlet and outlet is an essential step for dynamic melting. Any delay in commencing dynamic melting would mostly add to the overall charging time. Hence, as a disturbing factor, the fin halts the melting front's advancement due to the delay in commencing the dynamic melting. In fact, the fin, which is made of copper, has high thermal conductivity, but even the high thermal conductivity of the fin cannot replace the mixed convection flow and dynamic melting.

A long fin requires a long time to melt its surrounding NPCM and allow a forced convection flow of liquid PCM. Hence, a long fin demands 220 s until liquid film formation, and dynamic melting commences. However, reducing the fin's length to 1 mm (no fin) makes the film formation quick, and it takes only 1 min (60 s) to start dynamic melting. Moreover, increasing the fin's length delays the dynamic melting. It reduces the flow rate in the middle stages of melting, but, ultimately, the outlet flow rate is almost independent of fin length.

Figure 11 shows the influence of the nanoparticle concentrations on the heat transfer characteristics of the chamber during thermal charging. In this part, a fair configuration with a low inlet pressure (P_{in} = 500 Pa), high metal foam porosity (ε = 0.975), and moderate fin length (L_{fin} = 13 mm) were adopted to investigate the impact of nanoparticle concentration on the thermal charging behavior of the chamber.

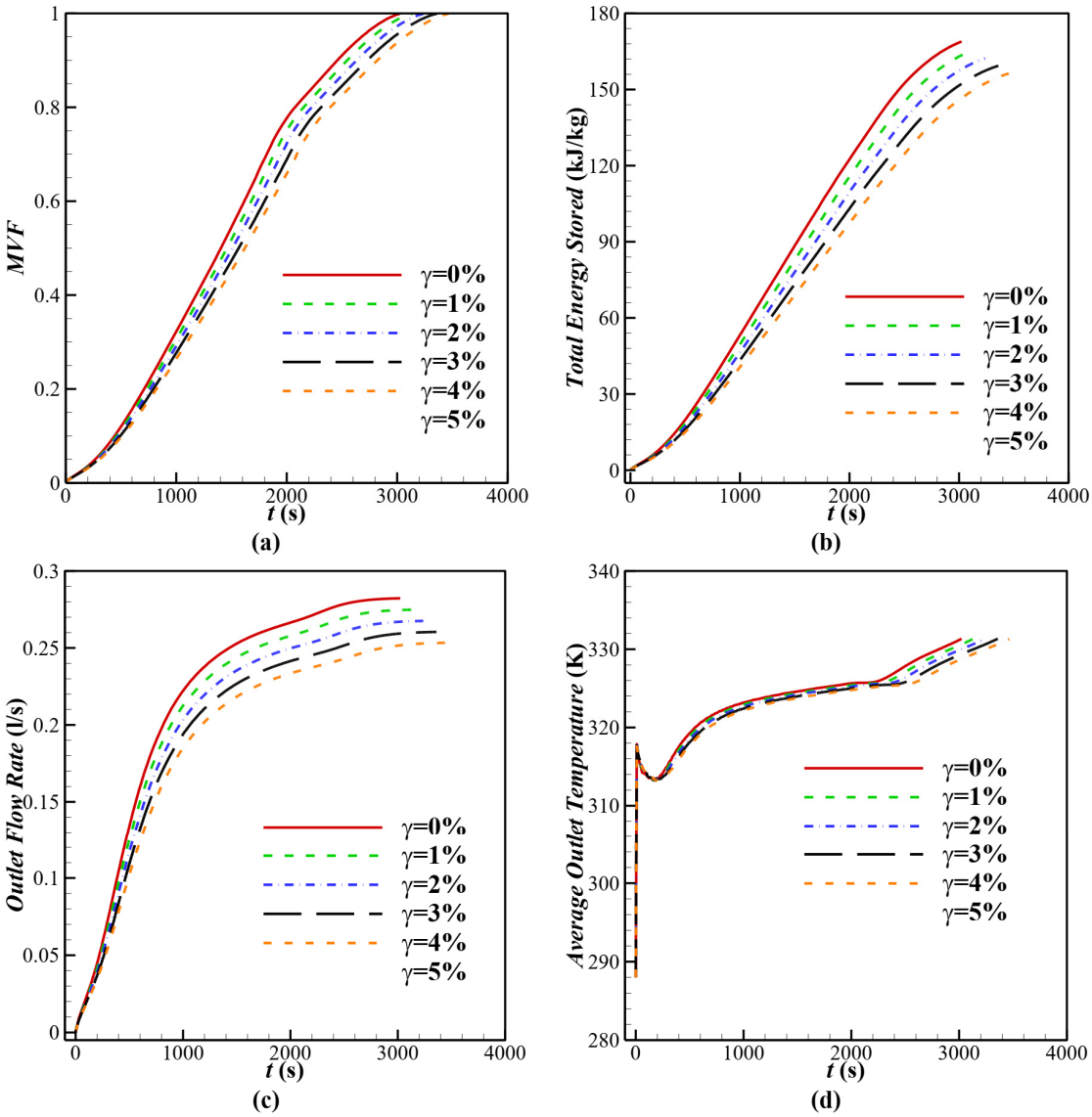

Figure 11. Effect of nanoparticle concentration on (**a**) melting volume fraction, (**b**) total stored energy, (**c**) flow rate, and (**d**) average outlet temperature.

Interestingly, the results show that a chamber filled with no nanoparticles (pure PCM) was fully melted faster than a similar case filled with NPCM. The nanoparticles' presence also reduced the chamber's thermal storage capacity since they do not contribute to latent-heat energy storage. The increase in the concentration of the nanoparticles also reduced the liquid NPCM flow rate in the chamber. The nanoparticles cannot contribute to latent-heat thermal energy storage, and hence, the latent-heat capacity of the NPCM is lower than a pure PCM. Moreover, the nanoparticles increase the dynamic viscosity of the PCM (see Equation (10d)), and, consequently, the friction forces in the metal foam rise and the flow rate drops. An NPCM containing nanoparticles has the advantage of better thermal conductivity compared to a pure PCM. However, such an advantage is minor in dynamic

melting compared to the flow rate reduction. Thus, it can be concluded that the presence of nanoparticles is not favorable for the thermal charging of a chamber with dynamic melting.

5. Conclusions

A new design for latent-heat thermal energy storage, dynamic melting, which benefits from a forced convection flow of NPCM, was addressed. In this design, pressurized liquid CuO–coconut oil enters a chamber from the bottom and leaves the chamber from the top. The chamber is filled with an open-cell copper foam. A copper fin was attached to the hot wall in the middle of the chamber to divert the hot flow of liquid NPCM and enhance the heat transfer. The enthalpy-porosity method and the finite element method were used to simulate the dynamic melting in the chamber. The effects of metal foam porosity, inlet pressure, the fin's length, and nanoparticle concentrations on the chamber's thermal characteristics were investigated. The isotherms and streamlines were also plotted and analyzed. The most important findings of the current research can be summarized as follows:

- Increasing the foam's porosity raises the amount of void space and weakens the effective thermal conductivity of NPCM–metal foam. Hence, increasing the porosity from 0.85 to 0.975 increases the thermal charging time of the chamber by about 10 min. An increase in porosity raises the thermal energy storage capacity of the chamber by providing a higher void space that the NPCM can fill. A porosity $\varepsilon = 0.95$ reduces the volume capacity of the chamber only by 2.5% compared to case $\varepsilon = 0.975$, but it fairly reduces the charging time by 25% compared to case $\varepsilon = 0.975$. Considering the energy storage power, an optimal value of 15.1 kW/kg was obtained for a porosity of $\varepsilon = 0.95$ since it benefits from good storage capacity and low charging time. Moreover, a foam with low porosity has low permeability and notable resistance to fluid flow. Thus, the flow rate in a foam with a porosity $\varepsilon = 0.85$ is 56% lower than that of $\varepsilon = 0.975$.
- Increasing the inlet's static pressure raises the flow rate of liquid NPCM flowing through the chamber and enhances the convective heat transfer. Increasing the inlet pressure from 500 Pa to 4000 Pa reduces the melting time by 22 min. The chamber's heat capacity is independent of the inlet pressure, but the charging time heavily depends on the inlet pressure. Thus, increasing the inlet pressure from 500 Pa to 4000 Pa increases the energy storage power by about 2.6 times.
- In the design of a chamber with dynamic melting, using a long fin as a flow divergent is not beneficial to the heat transfer and thermal charging of the chamber. A fin longer than 41 mm delays commencing the dynamic melting and extends the overall charging time.
- Dispersing nanoparticles in the pure PCM increases the thermal conductivity of the resulting NPCM, but it also increases the dynamic viscosity and reduces the heat capacity of the mixture. Since the dynamic melting is largely dependent on the forced convection flow of NPCM circulating the chamber, the increase in dynamic viscosity negatively impacts the heat transfer rate and extends the thermal charging time. Thus, using nanoparticles was not beneficial to the dynamic melting design.

Author Contributions: Conceptualization, M.G., H.A., O.Y., M.F., A.J.C., I.A.M. and A.O.A.; methodology, M.G., H.A., O.Y., M.F., A.J.C., I.A.M. and A.O.A.; software, M.G.; validation, M.G. and A.J.C.; formal analysis, M.G. and O.Y.; investigation, M.G., H.A., O.Y., M.F., A.J.C., I.A.M. and A.O.A.; resources, H.A.; data curation, M.G.; writing—original draft preparation, M.G., H.A., O.Y., M.F., A.J.C., I.A.M. and A.O.A.; writing—review and editing, M.G., H.A., O.Y., M.F., A.J.C., I.A.M. and A.O.A.; visualization, M.G. and A.J.C.; supervision, M.G. and A.J.C.; project administration, A.J.C.; funding acquisition, H.A. and A.J.C. All authors have read and agreed to the published version of the manuscript.

Funding: This research work was funded by the Institutional Fund Project under grant no. (IFPIP:1553-135-1442). Therefore, the authors gratefully acknowledge the technical and financial support from the Ministry of Education and King Abdulaziz University, DSR, Jeddah, Saudi Arabia.

Data Availability Statement: Not applicable.

Acknowledgments: This research work was funded by the Institutional Fund Project under grant no. (IFPIP:1553-135-1442). Therefore, the authors gratefully acknowledge the technical and financial support from the Ministry of Education and King Abdulaziz University, DSR, Jeddah, Saudi Arabia.

Conflicts of Interest: The authors declare no conflict of interest.

References

1. Abbasi, K.R.; Shahbaz, M.; Zhang, J.; Irfan, M.; Alvarado, R. Analyze the environmental sustainability factors of China: The role of fossil fuel energy and renewable energy. *Renew. Energy* **2022**, *187*, 390–402. [CrossRef]
2. Yang, X.; Xu, F.; Wang, X.; Guo, J.; Li, M.-J. Solidification in a shell-and-tube thermal energy storage unit filled with longitude fins and metal foam: A numerical study. *Energy Built Environ.* **2021**, *4*, 64–73. [CrossRef]
3. Yang, X.; Guo, J.; Yang, B.; Cheng, H.; Wei, P.; He, Y.-L. Design of non-uniformly distributed annular fins for a shell-and-tube thermal energy storage unit. *Appl. Energy* **2020**, *279*, 115772. [CrossRef]
4. Ghasemi, K.; Tasnim, S.; Mahmud, S. PCM, nano/microencapsulation and slurries: A review of fundamentals, categories, fabrication, numerical models and applications. *Sustain. Energy Technol. Assess.* **2022**, *52*, 102084. [CrossRef]
5. Yang, X.; Wang, X.; Liu, Z.; Luo, X.; Yan, J. Effect of fin number on the melting phase change in a horizontal finned shell-and-tube thermal energy storage unit. *Sol. Energy Mater. Sol. Cells* **2022**, *236*, 111527. [CrossRef]
6. Zhang, Y.; Bozorg, M.V.; Torres, J.F.; Zhao, Y.; Wang, X. Dynamic melting of encapsulated PCM in various geometries driven by natural convection of surrounding air: A modelling-based parametric study. *J. Energy Storage* **2022**, *48*, 103975. [CrossRef]
7. Liu, A.; Lin, J.; Zhuang, Y. PIV experimental study on the phase cshange behavior of phase change material with partial filling of metal foam inside a cavity during melting. *Int. J. Heat Mass Transf.* **2022**, *187*, 122567. [CrossRef]
8. Ami Ahmadi, H.; Variji, N.; Kaabinejadian, A.; Moghimi, M.; Siavashi, M. Optimal design and sensitivity analysis of energy storage for concentrated solar power plants using phase change material by gradient metal foams. *J. Energy Storage* **2021**, *35*, 102233. [CrossRef]
9. Bianco, N.; Busiello, S.; Iasiello, M.; Mauro, G.M. Finned heat sinks with phase change materials and metal foams: Pareto optimization to address cost and operation time. *Appl. Therm. Eng.* **2021**, *197*, 117436. [CrossRef]
10. Yang, X.; Yu, J.; Guo, Z.; Jin, L.; He, Y.-L. Role of porous metal foam on the heat transfer enhancement for a thermal energy storage tube. *Appl. Energy* **2019**, *239*, 142–156. [CrossRef]
11. Abishek, S.; King, A.J.C.; Nadim, N.; Mullins, B.J. Effect of microstructure on melting in metal-foam/paraffin composite phase change materials. *Int. J. Heat Mass Transf.* **2018**, *127*, 135–144. [CrossRef]
12. Nie, C.; Liu, J.; Deng, S. Effect of geometry modification on the thermal response of composite metal foam/phase change material for thermal energy storage. *Int. J. Heat Mass Transf.* **2021**, *165*, 120652. [CrossRef]
13. Dede, E.M.; Joshi, S.N. Thermal Management Systems Including Multiple Phase Changing Materials and Vehicles Including the Same. U.S. Patent No. 11,374,273, 31 October 2018.
14. Razack, S.K. Thermal Management System and Device. U.S. Patent No. 17/441,357, 19 May 2022.
15. Zheng, H.; Wang, C.; Liu, Q.; Tian, Z.; Fan, X. Thermal performance of copper foam/paraffin composite phase change material. *Energy Convers. Manag.* **2018**, *157*, 372–381. [CrossRef]
16. Prasanth, N.; Sharma, M.; Yadav, R.N.; Jain, P. Designing of latent heat thermal energy storage systems using metal porous structures for storing solar energy. *J. Energy Storage* **2020**, *32*, 101990. [CrossRef]
17. Khodadadi, M.; Sheikholeslami, M. Heat transfer efficiency and electrical performance evaluation of photovoltaic unit under influence of NEPCM. *Int. J. Heat Mass Transf.* **2022**, *183*, 122232. [CrossRef]
18. Hassan, M.; El-Zahar, E.R.; Khan, S.U.; Rahimi-Gorji, M.; Ahmad, A. Boundary layer flow pattern of heat and mass for homogenous shear thinning hybrid-nanofluid: An experimental data base modeling. *Numer. Methods Part. Differ. Equ.* **2021**, *37*, 1234–1249. [CrossRef]
19. Reddy, M.G.; Rani, S.; Kumar, K.G.; Seikh, A.H.; Rahimi-Gorji, M.; Sherif, E.-S.M. Transverse magnetic flow over a Reiner–Philippoff nanofluid by considering solar radiation. *Mod. Phys. Lett. B* **2019**, *33*, 1950449. [CrossRef]
20. Ali, R.; Asjad, M.I.; Aldalbahi, A.; Rahimi-Gorji, M.; Rahaman, M. Convective flow of a Maxwell hybrid nanofluid due to pressure gradient in a channel. *J. Therm. Anal. Calorim.* **2021**, *143*, 1319–1329. [CrossRef]
21. Leong, K.Y.; Abdul Rahman, M.R.; Gurunathan, B.A. Nano-enhanced phase change materials: A review of thermo-physical properties, applications and challenges. *J. Energy Storage* **2019**, *21*, 18–31. [CrossRef]
22. Li, Z.-R.; Hu, N.; Liu, J.; Zhang, R.-H.; Fan, L.-W. Revisiting melting heat transfer of nano-enhanced phase change materials (NePCM) in differentially-heated rectangular cavities using thermochromic liquid crystal (TLC) thermography. *Int. J. Heat Mass Transf.* **2020**, *159*, 120119. [CrossRef]
23. Li, Z.-R.; Fu, G.-T.; Fan, L.-W. Synergistic effects of nano-enhanced phase change material (NePCM) and fin shape on heat storage performance of a finned shell-and-tube unit: An experimental study. *J. Energy Storage* **2022**, *45*, 103772. [CrossRef]
24. Li, D.; Wu, Y.; Liu, C.; Zhang, G.; Arıcı, M. Numerical investigation of thermal and optical performance of window units filled with nanoparticle enhanced PCM. *Int. J. Heat Mass Transf.* **2018**, *125*, 1321–1332. [CrossRef]

25. Ho, C.J.; Guo, Y.-W.; Yang, T.-F.; Rashidi, S.; Yan, W.-M. Numerical study on forced convection of water-based suspensions of nanoencapsulated PCM particles/Al2O3 nanoparticles in a mini-channel heat sink. *Int. J. Heat Mass Transf.* **2020**, *157*, 119965. [CrossRef]
26. Ji, C.; Qin, Z.; Dubey, S.; Choo, F.H.; Duan, F. Simulation on PCM melting enhancement with double-fin length arrangements in a rectangular enclosure induced by natural convection. *Int. J. Heat Mass Transf.* **2018**, *127*, 255–265. [CrossRef]
27. Jmal, I.; Baccar, M. Numerical investigation of PCM solidification in a finned rectangular heat exchanger including natural convection. *Int. J. Heat Mass Transf.* **2018**, *127*, 714–727. [CrossRef]
28. Abdi, A.; Martin, V.; Chiu, J.N.W. Numerical investigation of melting in a cavity with vertically oriented fins. *Appl. Energy* **2019**, *235*, 1027–1040. [CrossRef]
29. Yazici, M.Y.; Avci, M.; Aydin, O. Combined effects of inclination angle and fin number on thermal performance of a PCM-based heat sink. *Appl. Therm. Eng.* **2019**, *159*, 113956. [CrossRef]
30. Nakhchi, M.E.; Esfahani, J.A. Improving the melting performance of PCM thermal energy storage with novel stepped fins. *J. Energy Storage* **2020**, *30*, 101424. [CrossRef]
31. Guo, J.; Liu, Z.; Du, Z.; Yu, J.; Yang, X.; Yan, J. Effect of fin-metal foam structure on thermal energy storage: An experimental study. *Renew. Energy* **2021**, *172*, 57–70. [CrossRef]
32. Zhang, C.; Yu, M.; Fan, Y.; Zhang, X.; Zhao, Y.; Qiu, L. Numerical study on heat transfer enhancement of PCM using three combined methods based on heat pipe. *Energy* **2020**, *195*, 116809. [CrossRef]
33. Joshi, V.; Rathod, M.K. Experimental and numerical assessments of thermal transport in fins and metal foam infused latent heat thermal energy storage systems: A comparative evaluation. *Appl. Therm. Eng.* **2020**, *178*, 115518. [CrossRef]
34. Senobar, H.; Aramesh, M.; Shabani, B. Nanoparticles and metal foams for heat transfer enhancement of phase change materials: A comparative experimental study. *J. Energy Storage* **2020**, *32*, 101911. [CrossRef]
35. Sheikholeslami, M.; Keshteli, A.N.; Shafee, A. Melting and solidification within an energy storage unit with triangular fin and CuO nano particles. *J. Energy Storage* **2020**, *32*, 101716. [CrossRef]
36. Kok, B. Examining effects of special heat transfer fins designed for the melting process of PCM and Nano-PCM. *Appl. Therm. Eng.* **2020**, *170*, 114989. [CrossRef]
37. Pássaro, J.; Rebola, A.; Coelho, L.; Conde, J.; Evangelakis, G.A.; Prouskas, C.; Papageorgiou, D.G.; Zisopoulou, A.; Lagaris, I.E. Effect of fins and nanoparticles in the discharge performance of PCM thermal storage system with a multi pass finned tube heat exchange. *Appl. Therm. Eng.* **2022**, *212*, 118569. [CrossRef]
38. Zuo, H.; Wu, M.; Zeng, K.; Zhou, Y.; Kong, J.; Qiu, Y.; Lin, M.; Flamant, G. Numerical investigation and optimal design of partially filled sectorial metal foam configuration in horizontal latent heat storage unit. *Energy* **2021**, *237*, 121640. [CrossRef]
39. Ghalambaz, M.; Mehryan, S.; Hajjar, A.; Shdaifat, M.Y.A.; Younis, O.; Talebizadehsardari, P.; Yaïci, W. Thermal charging optimization of a Wavy-shaped nano-enhanced thermal storage unit. *Molecules* **2021**, *26*, 1496. [CrossRef]
40. Li, M.-J.; Li, M.-J.; Xue, X.-D.; Li, D. Optimization and design criterion of the shell-and-tube thermal energy storage with cascaded PCMs under the constraint of outlet threshold temperature. *Renew. Energy* **2022**, *181*, 1371–1385. [CrossRef]
41. Mahdi, J.M.; Nsofor, E.C. Melting enhancement in triplex-tube latent heat energy storage system using nanoparticles-metal foam combination. *Appl. Energy* **2017**, *191*, 22–34. [CrossRef]
42. Sardari, P.T.; Mohammed, H.I.; Giddings, D.; Walker, G.S.; Gillott, M.; Grant, D. Numerical study of a multiple-segment metal foam-PCM latent heat storage unit: Effect of porosity, pore density and location of heat source. *Energy* **2019**, *189*, 116108. [CrossRef]
43. Ghalambaz, M.; Mehryan, S.; Mahdavi, M.; Younis, O.; Alim, M.A. Evaluation of the melting performance in a conical latent heat thermal unit having variable length fins. *Sustainability* **2021**, *13*, 2667. [CrossRef]
44. Al-Jethelah, M.; Ebadi, S.; Venkateshwar, K.; Tasnim, S.H.; Mahmud, S.; Dutta, A. Charging nanoparticle enhanced bio-based PCM in open cell metallic foams: An experimental investigation. *Appl. Therm. Eng.* **2019**, *148*, 1029–1042. [CrossRef]
45. Choi, S.-K.; Kim, S.-O.; Lee, T.-H.; Dohee-Hahn. Computation of the natural convection of nanofluid in a square cavity with homogeneous and nonhomogeneous models. *Numer. Heat Transf. Part A Appl.* **2014**, *65*, 287–301. [CrossRef]
46. Schenk, O.; Gärtner, K. Solving unsymmetric sparse systems of linear equations with PARDISO. *Future Gener. Comput. Syst.* **2004**, *20*, 475–487. [CrossRef]
47. Wriggers, P. *Nonlinear Finite Element Methods*; Springer Science & Business Media: Berlin, Germany, 2008.
48. Kamkari, B.; Shokouhmand, H.; Bruno, F. Experimental investigation of the effect of inclination angle on convection-driven melting of phase change material in a rectangular enclosure. *Int. J. Heat Mass Transf.* **2014**, *72*, 186–200. [CrossRef]